Targeted insult to individual subsurface cortical blood vessels using ultrashort laser pulses: Three models of stroke

Nozomi Nishimura[1,4], Chris B. Schaffer[1,4], Beth Friedman[2], Philbert S. Tsai[1,4], Patrick D. Lyden[2,3] and David Kleinfeld[1,3,4]

[1]Department of Physics
[2]Department of Neurosciences
[3]Graduate Program in Neurosciences
[4]Center for Theoretical Biological Physics
University of California at San Diego
La Jolla, CA 92093

Figures:	7 (all in color)
Abstract:	180 words
Main text:	4,700 words
References	49

Correspondence: David Kleinfeld
Department of Physics 0374
University of California
9500 Gilman Drive
La Jolla, CA 92093
Office: 858-822-0342
Fax: 858-534-7697
Email: dk@physics.ucsd.edu

ABSTRACT

To assess redundancy in vascular flow and to model microvessel diseases, we present a method to produce vascular disruptions within rat brain parenchyma that targets single microvessels. Two-photon microscopy was used to image vascular architecture, select a vessel for injury, and measure blood flow dynamics. We irradiated the vessel with high-fluence, ultrashort laser pulses. Three forms of vascular insult were achieved: (*i*) Vessel rupture was induced at the highest optical energies. This provides a model for hemorrhage. (*ii*) Extravasation of blood components was induced near the lowest energies and is accompanied by maintained flow in the target vessel. (*iii*) An intravascular clot evolved when an extravasated vessel was further irradiated. Such clots dramatically impaired blood flow in downstream vessels, where average speeds dropped as low as ~ 10 % of baseline values. This demonstrates that a single blockage to a microvessel can lead to local cortical ischemia. Lastly, the spatially restricted nature of the microvascular clot was exploited to study the consequences of hemodilution on perfusion. We found that a reduction in hematocrit led to a restoration of flow in secondary downstream vessels.

Brain homeostasis depends on adequate levels of blood flow to ensure the delivery of nutrients to brain cells and to facilitate the removal of metabolites and heat. In the cerebral cortex, the vasculature forms networks of subsurface microvessels. In principle, these networks provide multiple routes for blood to flow to the same cortical column[1-4]. Interestingly, these microvessels are an important locus of cerebral vascular disease, as their dysfunction contributes to cognitive impairment in disorders such as vascular dementia, Alzheimer's disease, and "silent" stroke[5-7]. However, the development of models of microvessel dysfunction has been problematic as it has been difficult to selectively target and lesion cerebral microvessels, which reside deep to the surface of the brain.

There are several forms of vascular dysfunction that can contribute to the onset of blood flow disturbances and neurodegeneration[8,9]. One form is a vascular leak that leads to extravasation of serum proteins into the cerebral space and brain antigens into the peripheral circulation. This can occur as a result of inflammation that alters the vessel glycocalyx and tight junctions that normally help maintain the blood-brain barrier. Another form of vascular dysfunction occurs when there is a sudden rupture of a vessel; this leads to hemorrhage and rapid spillage of vessel contents into the brain parenchyma. A third type of vascular dysfunction is caused by vessel occlusion, which leads to ischemia.

As a means to perturb microvessels in the parenchyma without affecting the surrounding area, we introduce *in vivo* photodisruption of a targeted, deep-lying vessel. Our approach is motivated by past optically-based studies[10,11] and shaped by recent developments in the nonlinear interaction of light and matter. Nonlinear interactions achieved with high-energy, ultrashort pulses of light at the focus of an objective lead to ionization within a femtoliter-sized volume, which leads to the spatially-limited release of mechanical energy[12]. This suggests the utility of ultrashort laser pulses to directly disrupt vascular cells deep to the cortical surface with minimal collateral damage. A second motivation is the natural integration of photodisruption by high-energy laser light and the imaging of fluorescently-labeled tissue at low energy by two-photon laser

scanning microscopy (TPLSM)[13,14], to map the topology and speed of blood flow in surrounding vessels. This combination enables the targeting and real-time monitoring of the photodisruption of individual blood vessels.

RESULTS

Our preparation was the adult rat with an observation window placed over parietal cortex. The underlying vasculature was imaged with *in vivo* TPLSM (**Fig. 1a**), which relies on contrast generated by labeling of the blood plasma with high molecular weight fluorescein-dextran. Vessels throughout the cranial window were first mapped at low-magnification. We acquired planar images of the fluorescent intensity at successive depths in the cortex, which were transformed into maximal projections. Projections from several neighboring regions were knitted together to form a single map of an area of the exposed brain (**Fig. 1b**). Target vessels for photodisruption were selected using the criteria that a portion of the vessel coursed parallel to the cortical surface. The vessels comprised parenchymal arterioles, venules and capillaries, with a range of diameters from 5 to 25 μm and subsurface depths of 30 to 480 μm. Capillaries were identified by their small diameter, *i.e.*, 5 to 7 μm. To aid in the classification of larger target vessels as arteriole or venule, we traced the shortest path from the target to a surface vessel that was identifiable as a vein or artery.

Once a target was selected and classified, we mapped the local vascular architecture in the vicinity of the target vessel with a three-dimensional stack of high-magnification images (**Fig. 1c**). We further measured the red blood cell (RBC) velocities in the target vessel and neighboring vessels before and after photodisruption with repetitive line scans[14]. Alternatively, the speed of RBCs could be ascertained from the planar images by the orientation of streaks formed by the motion of RBCs.

Insult to the targeted vessel was generated by irradiation of the lumen of the vessel with controlled numbers and energies of amplified, ~ 100-fs duration pulses of laser light. This process was simultaneous with planar imaging and provided real-time feedback on the progress of the photodisruption (**Fig. 1a**). The first indication of photodisruption was

visualized as the accumulation of fluorescein-dextran outside the vessel lumen. This corresponds to extravasation. In general, the incident pulse energy required to initiate extravasation was at least 0.03 μJ, which corresponds to a threshold fluence for damage of ~ 1 J/cm^2 at the focus, consistent with literature values[12]. Deeper vessels and those lying beneath larger blood vessels required relatively higher incident energies. Changing the focus location from the lumen to the vessel walls did not affect the extravasation; therefore, we minimized the potential effects of laser light on neuronal tissue by focusing into the vessel lumen.

Three forms of vascular disruption were generated (**Fig. 1d**). High laser pulse energies resulted in hemorrhages with ruptured vasculature. At low laser pulse energies, we achieved two types of vascular disruption that left the target vessel intact: extravasations with continued blood flow and clots with complete vessel occlusion.

Vessel rupture

The most drastic of the insults was the rupture of the target vessel, which led to a hemorrhage of blood plasma and RBCs into the parenchyma (**Fig. 2**). In these cases, irradiation with laser pulse energies that were well in excess of the threshold value for extravasation was immediately followed by an explosive expansion of fluorescently-labeled plasma into the extravascular tissue. A spherical “core” was often distinguishable from an irregularly shaped volume of fluorescent extravasation as early as 1 s after irradiation. Vessels in the core of the hemorrhage appeared to be completely disrupted. In contrast, intact vessels with moving RBCs were observed within the volume of extravasation that surrounds the core. Lastly, the size of the core rapidly stabilized (**Fig. 2b,c**) while the extravasation in the tissue that surrounds the core continued to expand for tens of seconds.

Across 17 hemorrhaged vessels in 10 animals, 1 to 10 pulses were delivered in a single train with an energy per pulse that ranged from 0.2 to 1 μJ. The mean value of 0.8 μJ was equivalent to about 30-times the threshold level. The initial radius of the hemorrhage core was found to scale linearly with the pulse energy (supplemental

material). The extravasation of fluorescent blood plasma and isolated RBCs extended beyond the core of the hemorrhage and achieved a radius of 90 ± 40 μm (mean ± SD). The final volume of extravasation, ~ 10^3 to 10^4 pL, was independent of the diameter of the vessel and the initial RBC speed (**Fig. 2d,e**).

Post mortem sections showed that the inner core is filled with RBCs (**Fig. 2f**). Scattered RBCs formed an irregularly-shaped hemorrhage that extended from the core. Further, nearby vessels appear to be filled with thrombi that breach vessel walls (**Fig. 2f,g**). Immunostaining with antibodies against MAP2 demonstrated preserved microtubule integrity in neuropil that is contiguous to the hemorrhage and extravasation site (**Fig. 2h**).

Extravasation

Reduced laser pulse energies allowed fine control of the vascular lesions. Beginning at a low level of energy, if no vascular changes were observed, the irradiation was repeated at the same or increased pulse energy until some extravasation of blood plasma was observed. This led to an insult in which the target vessel leaked blood plasma and often RBCs into the extravascular tissue, but remained intact with uninterrupted blood flow (**Fig. 3a**). The radius of the initial extravasation of plasma varied from constrained leakage within several micrometers of the vessel lumen (**Fig. 3b**) to leakage that extended tens of micrometers into the parenchymal tissue. Limited amounts of additional irradiation, in some cases with increased energy, resulted in further increases in the radius of extravasation (**Fig. 3b,c**). The blood flow within the vessels continued throughout the irradiation and leakage of vessel (**Fig. 3c**).

The final incident optical energies that we used to induce extravasation were typically 2- to 3-times times greater than the threshold energy and in the range of 0.1 to 0.5 μJ and were delivered in trains of 10 to 100 pulses (12 vessels in 10 rats). The measured RBC speed after extravasation was found to be 60 ± 20 % of the baseline value (5 vessels in 5 animals; we observed an additional case in which the target vessel doubled in RBC speed after extravasation). In all cases, the leakage of plasma from the target vessel

stabilized within minutes. The radial distances from the target vessel to the edge of extravasated fluorescein, as judged from planar images, achieved a steady-state value of 40 ± 30 μm. The measured volume of extravasation, ~10^2 to 10^3 pL, was not correlated with vessel diameter speed, initial RBC speed, or with the depth of the vessel (**Fig. 3d-f**).

Post-mortem sections from the level of the extravasation were identified by observation of a residual volume of fluorescent labeling in the parenchyma (**Fig. 3g**). Subsequent staining for RBCs indicated that by the time of sacrifice, 3 hours after vessel targeting, the extravasation sites are also marked with small aggregates of RBCs (**Fig. 3h**). Immunostaining with antibodies against MAP2 shows numerous stained neurons that are contiguous to the center of extravasation. Importantly, the volume of tissue superficial to the disrupted vessel is also immunostained, supporting the realization of subsurface targeting.

Intravascular clot

The procedure and laser pulse energies used to produce ischemic clots was an extension of that used to induce extravasation (**Fig. 4**). Subsequent to the onset of extravasation, the irradiation was repeated with increased pulse energy and increasing number of pulses until there was a complete cessation of RBC movement in the target vessel (**Fig. 4b,c**). Immediately after irradiation, the vessel lumen swelled and there was a momentary lack of RBC motion, followed by a restoration of flow. Additional irradiation led to further extravasation, evidenced by the emergence of bright fluorescent patches outside the lumen of the vessel (**Fig. 4b**), and ultimately to clot formation, which was visualized as a non-fluorescent mass within the vessel (**Fig. 4b**). Measurements of the RBC speed during the photodisruption process showed several transient stops in the flow before a stable clot was formed (**Fig. 4c**); this clot was observed to remain intact 4 hours after irradiation.

Clot formation was achieved in 61 microvessels (39 animals) as deep as 480 μm below the surface. In addition, we independently demonstrated clot formation in pial vessels

up to 120 μm in diameter but extensive extravasation from surface vessels made it difficult to visualize vascular dynamics. Across all clots, the final volume of extravasation varied between 10 and 10^4 pl (**Fig. 4d**) and the volume was independent of the diameter of the vessel, the depth of the vessel, and the energy at the focus (**Fig. 4e,f,h**). There was a weak but statistically significant increase in volume as a function of the initial RBC speed (**Fig. 4g**).

The intravascular clot was identified in *post mortem* tissue sections from aggregates of RBCs (**Fig. 5a,b**) surrounded by a cloud of extravasated fluorescein-dextran (**Fig. 5c**). In this representative example, which includes 3 hours of survival after induction of the clot, immunostaining of MAP2 is present in the neuropil adjacent to the aggregates. The neuronal somata exhibited a range of pathology from cells that appear normal (asterisks in **Fig. 5d**) to cells with angulation of cell bodies, an indication of early neuronal pathology (arrows in **Fig. 5d**). As MAP2 immunostaining can be dynamically down-regulated within 1 hour of ischemia consequent to large vessel occlusion[15], it is notable that this had not obviously occurred within a 3 hour survival time (**Fig. 5a**) after clot formation.

A histological examination for vascular pathology focused on the region containing the clotted vessel. Anti-fibrin immunoreactivity, a known marker for clotting activity, could be observed in targeted vessels. For the vessel imaged in **Figure 6e**, the fibrin formed a dense core deposit with a more diffuse surround (**Fig. 6f**). This immunostaining was highly overlapped with the extravasated fluorescein in this section (**Fig. 6g**). The dense fibrin core appears associated with a vessel (**Fig. 6h,i**) whose size, orientation and position is consistent with the *in vivo* site of the clotted vessel (**Fig. 6e**). To assay potential damage to perivascular elements, we immunostained for the astrocyte protein vimentin, as this protein is strongly up-regulated in reactive astrocytes that proliferate in response to injury[16]. Vimentin appeared evenly distributed across the cortex with no increase in staining among those vessels adjacent to the clot (**Fig. 6j,k**).

Finally, we assessed acute ischemic effects across cell types with the hypoxia marker pimonidazole hydrochloride (Hypoxyprobe); this probe labels viable but oxidatively stressed tissue[17]. Hypoxyprobe staining was increased in the limited region of fluorescein-dextran extravasation near the clot (**Fig. 5l,m**).. *In toto*, these data indicate that clot formation results in a restricted zone of neural pathology (6 clots across 5 animals).

Selectivity of vascular insult

The above definitions of vascular insults offer a convenient categorization scheme, but the observed effects encompass a continuum of effects. Hemorrhages could always be attained at high laser energies (**Fig. 2**). The disruption obtained at low energies (85 vessels) was variable. In 8 of the vessels, the initial response was extravasation that rapidly evolved into a clot in the absence of additional pulses, while in 10 of the vessels the initial response was an unplanned hemorrhage. Stable extravasation was achieved in the remaining 67 vessels. In the absence of further laser pulses, flow was observed for at least several minutes (14 vessels) (**Fig. 3**). With additional irradiation, a clot formed that completely stopped RBC motion (53 vessels) (**Fig. 4**). Although our method does not guarantee the choice of vascular insult, the real-time monitoring of the vasculature with TPLSM assures that the investigator will be able to fully characterize the actual insult.

Blood flow dynamics after a single intravascular clots.

To demonstrate the novel capabilities of our methodology, we investigated the changes in RBC flow in subsurface vascular networks that occurred after clot induction. The target vessels consisted of both fine arterioles, 7 to 9 μm in diameter (6 of 8 animals), and capillaries, ~ 5 μm in diameter (2 of 8 animals). The arterioles were 1 to 2 branches downstream from diving arterioles, as identified by their connectivity with surface arteries, and the capillaries were at least 4 branches away from surface arteries. Data from 3 examples are shown in **Figure 6a-c**. Prior to photodisruption, we measured the direction and speed of baseline RBC flow in vessels contiguous to the target vessel (X) in order to construct vessel-by-vessel flow maps (1st and 2nd columns,

Fig. 6a-c). These measurements were repeated immediately after a stable clot was formed in the target vessel (3rd and 4th columns, **Fig. 6a-c**). In all cases, the direction of flow in the upstream and parallel vessels was unchanged by the clot and the magnitude of baseline and post-clot velocities were similar. In contrast, flow in the downstream vessels was often reversed in direction and significantly reduced in magnitude.

We compiled the RBC speeds across all cases. The vessels we observed were categorized by their relation to the target, *i.e.*, vessels that lay upstream (U), parallel (P), one and two branches downstream (D1 and D2), and three and four branches downstream (D3 to D4) of the target vessel (**Fig. 6d**). In upstream and parallel vessels, the preservation of post-clot RBC speed was demonstrated by a distribution of values close to 100 % of the baseline value (**Fig. 6e**). In contrast, the mean post-clot RBC speeds in primary and secondary downstream vessels decreased in magnitude to 7 % (0 to 5 % across the lowest three quartiles) and 40 % (0 to 27 %) of their respective baseline values (**Fig. 6f**). The mean post-clot RBC speeds in vessels three and four branches downstream were indistinguishable and reduced to 45 % (0 to 67 %) of the baseline value (**Fig. 6g**). In general, the decrement in RBC speed in downstream vessels encompassed vessels well outside the extent of extravasation around the target vessel. Interestingly, flow in contiguous vessels that were not supplied by the target were largely unaffected by the occlusion (*e.g.*, asterisk in **Fig. 6b**).

Restoration of flow after a clot. The localized nature and stability of the subsurface ischemic blockages allowed us to assess possible reperfusion that results from a clinically motivated treatment. We consider two complementary approaches. The first makes use of hypervolumetric hemodilution[18] as a means to reduce the hematocrit and thus the viscosity of the blood. The second makes use of agents that can dissolve clots in otherwise normal vessels[19,20].

Subsequent to clot formation and a reduction in the downstream flow of RBCs (**Fig. 4 and 6**), we diluted the blood through the injection of isotonic saline over a period of ~ 30 minutes. We observed a partial restoration of the flow downstream from the occluded

vessel, as illustrated by the example of **Figure 7a**. Across a population (8 animals and 55 vessels), those vessels that lay immediately downstream of the occlusion, *i.e.*, D1, slowed to less than 10 % of baseline speed during the occlusion and were essentially unaffected by hemodilution (**Fig. 7b,d**). In marked contrast, the flow in vessels that lay one additional branch point away from the occlusion, *i.e.*, D2 branches, slowed to approximately 20 % of the baseline speed during the occlusion yet almost completely recovered subsequent to hemodilution (**Fig. 7b,d**). Flow in the D3 and D4 branches was only mildly reduced by the clots (**Fig. 6g**), although flow was partially restored by hemodilution for these cases as well (**Fig. 7b,d**).

We checked if hemodilution *per se* could significantly increase flow irrespective of the initial clot. The result of control experiments shows that the flow of RBCs in neighboring blood vessels that maintained a separate source from the occluded vessel were essentially unaffected by the clot. The flow in these vessels, located 0.3 to 1 mm away from the occluded vessel, showed a slight but statistically insignificant increase in speed subsequent to hemodilution (**Fig. 7c,d**).

In the second approach to increase flow after a clot, we attempted to dissolve the clot with recombinant tissue-type plasminogen activator (r-tPA). In 10 animals, r-tPA was infused into the blood after single vessel occlusion (12 occlusions). Peripheral bleeding indicated successful injection and successful r-tPA injection was confirmed by the immunohistological labeling for r-tPA in sections of brain tissue in the vicinity of the clot (5 of 5 animals). In all cases the vessels remained occluded after r-tPA injections (data not shown). Lastly, we performed 3 experiments in which we clotted vessels before (4 vessels) and after (8 vessels) the injection of heparin. Heparin did not affect the existing clots or prevent the formation of clots (data not shown).

DISCUSSION

We have demonstrated a method using unltrashort pulses of near-infrared laser light for the production of injury to single parenchymal microvessels within the superficial layers

of rat cortex while preserving the overlying vasculature. Three types of vascular insult were demonstrated (**Fig. 1d**), 1) a high energy induced nanoliter sized hemorrhage, 2) a low energy induced vessel breach with extravasation of less than one nanoliter and continued flow of ~ 60 % of the baseline value and 3) a multiple low energy pulse induced clot.

Two clinical therapies used for major stroke were evaluated using the intravascular clot model. Clinical trials have demonstrated occlusions in humans that are unresponsive to thrombolytic therapy, of which r-tPA is a commonly used agent[19,21]. Similarly, occlusions generated with our technology do not respond to treatment with r-tPA. The manipulation of flow by hemodilution, to decrease the apparent viscosity of the blood[22], has been shown to be of clinical use as a treatment for large-scale strokes[18]. Our results suggest that such strategies may be an effective means to increase flow around small vessel occlusions.

The high connectivity in brain vascular networks could aid in providing a "fail-safe" mechanism to maintain flow after blockages[3,23]. Recent data shows that this conjecture is borne out in the network of surface arterioles, where only a small decrease in blood flow is observed downstream from a clotted vessel [24]. In contrast, we studied deep-lying microvascular networks and found a substantial decrease in RBC speed in vessels that lie downstream from an intravascular clot. The severe drop in blood flow immediately downstream from the clot could reflect distal effects of pathology associated with the clot, such as inflammatory or electrically mediated microvessel constriction. While we cannot rule out these mechanisms, the persistent nature of flow during extravasation (**Fig. 3c**) suggests that the changes in blood flow subsequent to vessel occlusion are caused largely by the localized clot. This suggests that the reduction in downstream flow after a clot is a consequence of the topology of the subsurface vascular network and the fluid mechanics of blood flow. Further support for this interpretation comes from the dramatic reperfusion that occurs in secondary vessels upon hemodilution (**Fig. 7d**). Independent of mechanism, a 90 % drop in cortical blood flow that is induced by blockage of a large artery, even for a short duration, is sufficient

to cause neurological damage[25-27]. Thus our data suggests that clots in a single microvessel could lead to small localized lesions in the brain, such as lacunnes[28], and that hemodilution may be a means to restrict the extent of this lesion.

Mechanism for vascular damage

Past work has shown that the mechanical disturbance that is induced by nonlinear absorption of ultrashort pulses consists of a cavitation bubble and a shock wave. The size and strength of these disturbances depend on the laser energy absorbed by the tissue[12]. Interestingly, the spherical shape of the hemorrhagic core that follows vessel rupture is consistent with such a mechanism (supplemental material). For the cases of extravasation and clot formation, which occur at energies close to the damage threshold, the cavitation bubble and shock wave are hypothesized to be too weak to cause vessel rupture but sufficient to stress endothelial cells and the basement membrane and trigger the endogenous clotting cascade.

Relation to other neurovascular disease models

The present study complements past work that focused on large ischemic and hemorrhagic disruptions, which helped define the molecular basis for neurovascular pathology. This includes the induction of failures in the blood-brain barrier by the injection of agents that weaken vessels or disrupt the blood-brain barrier[29-31]. A prior approach to model hemorrhages made use of the injection of blood or blood constituents directly into the parenchyma[32]. This has the advantage of good spatial localization, yet the volume of the hemorrhage is relatively large. Our induction of blood extravasation may provide a unique means to model microbleeds, *i.e.,* localized, small hemorrhages observed in aged human patients[33].

Occlusion of large surface vessels has been variously modeled via the surgical insertion of a filament[34,35], ligation[36], or the optical irradiation of large surface vessels in conjunction with a blood-born photosensitizer[37,38]. Existing models of small ischemic strokes involve the intravascular injection of small clotting agents, such as microspheres[39] or pre-formed emboli[40], or the *in situ* formation of emboli[41]. Such

models have been of proven use for pre-clinical efficacy studies of therapeutic agents, yet are a challenge for real-time studies since the locations and extent of the occlusions can be variable. Our methodology obviates many of these difficulties and provides a useful tool to perturb and measure neurovascular coupling, a long-standing challenge in stroke research[42].

METHODS

Surgical preparation

Our subjects were 55 male Sprague-Dawley rats, 100 to 350 g in mass, that were anesthetized by interperitoneal injection of urethane (150 mg per 100 g rat), supplemented as necessary. Atropine sulfate was delivered by subcutaneous injection (5 μg per 100 g rat) at the start of surgery and supplemented hourly (1 μg per 100 g rat). We further supplemented with 5 % (w/v) glucose in physiological saline (0.5 ml per 100 g rat) every hour. Body temperature was maintained at 37.5° C with a heating blanket (no. 50-7053; Harvard) and blood oxygen levels and heart rate were monitored in a subset of animals with a pulse oxymeter (no. 8600V; Nonin). A 4 mm by 6 mm craniotomy was prepared over parietal cortex. The dura was removed, a chamber consisting of a metal frame and a removable glass coverslip (no. 1) lid was glued to the skull and the space between the exposed brain surface and the coverglass was filled with 1.5 % (w/v) agarose (no. A-9793, Sigma) in an artificial cerebro-spinal fluid[43]. To visualize the vasculature and the motion of RBCs with TPLSM, ~ 0.3 ml of a 5 % (w/v) solution of 2 MDa fluorescein-conjugated dextran (FD-2000S; Sigma) in physiological saline was injected intravenously. The care and experimental manipulation of our animals have been reviewed and approved by the Institutional Animal Care and Use Committee.

Two-photon laser scanning microscopy

Images were obtained with a two-photon laser scanning microscope of local design[44] that was modified to include an amplified beam (Fig. 1A)[45]. A 0.12-NA, 5X-magnification air objective (Olympus) was used to obtain images of the surface vasculature across the entire cranial window to aid in navigating around the cortical vasculature. We changed to a 0.8-NA, 40X, water-immersion objective (Olympus) for high-resolution imaging, line-scan measurements, and

photodisruption. The energy per pulse of the imaging beam never exceeded an incident value of 1 nJ on cortex.

Individual planar images that spanned the area surrounding the target vessel, or sets of images at 1-μm axial spacing, were obtained both before and after photodisruption. Planar images were also used to monitor the production of the vascular disruptions in real-time. Line scans along single vessels, with a maximum scan rate of 1.3 kHz, were used to quantify RBC velocity[14]. In some cases, RBC velocity was extracted from frames of images in which the fast-scanning axis of the imaging beam was aligned with the vessel axis and the distance between successive scans along the slow-scanning axis was small compared to the size of an RBC. Here, the motion of RBCs results in diagonal streaks in the image and the slope of the streak is inversely proportional to the RBC velocity.

Photodisruption

Photodisruption of microvasculature made use of high energy pulses that were generated with a multi-pass Ti:Al_2O_3 amplifier of local construction that followed the design of Backus *et al.*[46] and operated at a 1 kHz pulse-rate. The photodisruption beam and the imaging beam were combined before the microscope objective with a polarizing beamsplitter (Fig. 1A). The two beams were focused in the same focal plane and the amplified beam was centered in the area that is raster-scanned by the imaging beams so that photodisruption occurred at the center of the TPLSM imaged field. The energy per pulse of the photodisruption beam was varied with neutral density filters and the number of pulses was controlled by a mechanical shutter (Uniblitz no. LS3Z2 shutter and no. VMM-D1 driver; Vincent). The energy and number of pulses was modified based on damage assessed from the real-time TPLSM images.

Hemodilution

A drop in hematocrit was achieved by the uniform injection of 35 mL of saline per kg rat, *i.e.*, one-half of the estimated blood volume, into the tail vein or the femoral vein over a period of 30 minutes. This results in a reduction in hematocrit to 90 % of the baseline value (3 animals), as assayed by packed cell volume, at the end of 30 minutes.

Anticoagulants

In a selected group on animals, r-tPA (Genetech) was injected via the tail vein (4 animals) or via the carotid artery (6 animals) after clots were observed to be stable for 30 minutes. The rate of

injection was 10 mg per kg rat per hour and was continued until the r-tPA caused bleeding to appear at the cranial window. The final dosage varied between 6.3 and 23 mg per kg rat with an average 13 mg per kg rat. This dosage is higher than the typical dose of 5 to 10 mg per kg rat administered to break clots in the middle cerebral artery[47,48]. Heparin (no. 2440-41, Elkiins-Sinn) was injected intraveneously at 100 units per rat.

Additional methods

Our methods for the estimation of extravasation volume and *post mortem* analysis, which includes Hypoxyprobe-1 labeling and immunohistochemistry, are described in Supplementary Methods.

Acknowledgements

We thank Qun Cheng for assistance with the plasminogen activator experiments, Earl Dolnick for assistance with the electronics, Don Pizzo and Leon Thal for use of their photomicroscope, Lee Schroeder and Steven Siegel for discussions, and Coherent, Inc. for the loan of equipment. This work was funded by the David and Lucille Packard Foundation, the National Science Foundation (DBI/0455027), the National Institutes of Health (NS/041096, NS/043300, EB/003832, and RR/021907), a La Jolla Interfaces in Science Postdoctoral Fellowship to C.B.S., and a National Science Foundation Graduate Fellowship to N.N.

REFERENCES

1. Hudetz, G. A. Percolation phenomenon: The effect of capillary network rarefaction. *Microvascular Research* **45**, 1-10 (1993).
2. Moody, D. M., Bell, M. A. & Challa, V. R. Features of the cerebral vascular pattern that predict vulnerability to perfusion or oxygenation deficiency: An anatomic study. *American Journal of Neuroradiology* **11**, 431-439 (1990).
3. Brozici, M., van der Zwain, A. & Hillen, B. Anatomy and functionality of leptomeningeal anastomoses: A review. *Stroke* **34**, 2750-2762 (2003).
4. Cox, S. B., Woolsey, T. A. & Rovainen, C. M. Localized dynamic changes in cortical blood flow with whisker stimulation corresponds to matched vascular and neuronal architecture of rat barrels. *Journal of Cerebral Blood Flow and Metabolism* **13**, 899-913 (1993).
5. Iadecola, C. Neurovascular regulation in the normal brain and in Alzheimer's disease. *Nature Reviews of Neuroscience* **5**, 347-360 (2004).
6. Wardlaw, J. M., Sandercock, P. A., Dennis, M. S. & Starr, J. Is breakdown of the blood-brain barrier responsible for lacunar stroke, leukoaraiosis, and dementia? *Stroke* **34**, 806-812 (2003).
7. Cullen, K. M., K., Z. & Stone, J. Pericapillary haem-rich deposits: Evidence for microhaemorrhages in aging human cerebral cortex. *Journal Cerebral Blood Flow and Metabolism* **25**, 1656-1667 (2005).
8. del Zoppo, G. J. Microvascular changes during cerebral ischemia and reperfusion. *Cardiovascular and Brain Metabolism Reviews* **6**, 47-96 (1994).
9. Farkas, E. & Luiten, P. G. M. Cerebral microvascular pathology in aging and Alzheimer's disease. *Progress in Neurobiology* **64**, 575-611 (2001).
10. Watson, B. D., Dietrich, W. D., Busto, R., Wachtel, M. S. & Ginsberg, M. D. Induction of reproducible brain infarction by photochemically initiated thrombosis. *Annals of Neurology* **17**, 497-504 (1985).
11. Haseldonckx, M., van Bedaf, D., van de Ven, M., van Reempts, J. & Borgers, M. Vasogenic oedema and brain infarction in an experimental penumbra model. *Acta Neurochirurgica (Supplement)* **76**, 105-109 (2000).
12. Vogel, A. & Venugopalan, V. Mechanisms of pulsed laser ablation of biological tissues. *Chemical Reviews* **103**, 577-644 (2003).
13. Svoboda, K., Denk, W., Kleinfeld, D. & Tank, D. W. In vivo dendritic calcium dynamics in neocortical pyramidal neurons. *Nature* **385**, 161-165 (1997).
14. Kleinfeld, D., Mitra, P. P., Helmchen, F. & Denk, W. Fluctuations and stimulus-induced changes in blood flow observed in individual capillaries in layers 2 through 4 of rat neocortex. *Proceedings of the National Academy of Sciences USA* **95**, 15741-15746 (1998).
15. Dawson, D. A. & Hallenbeck, J. M. Acute focal ischemia-induced alterations in MAP2 immunostaining: Description of temporal changes and utilization as a marker for volumetric assessment of acute brain injury. *Journal of Cerebral Blood Flow and Metabolism* **16**, 170-174 (1996).
16. Latov, N. et al. Fibrillary astrocytes proliferate in response to brain injury. *Developmental Biology* **72**, 381-384 (1979).
17. Chapman, J. D., Franko, A. J. & Sharplin, J. A marker for hypoxic cells in tumours with potential clinical applicability. *British Journal of Cancer* **43**, 546-550 (1981).
18. Asplund, K. Haemodilution for acute ischaemic stroke (a review). *The Cochrane Library* **3**, 1-41 (2005).
19. Sakharov, D. V., Barrett-Bergshoeff, M., Hekkenberg, R. T. & Rijken, D. C. Fibrin-specificity of a plasminogen activator affects the efficiency of fibrinolysis and responsiveness to ultrasound: Comparison of nine plasminogen activators in vitro. *Thrombosis and Haemostasis* **81**, 605-612 (1999).
20. GUSTO_Investigators. The effects of tissue plasminogen activator, streptokinase, or both on coronary-artery patency, ventricular function, and survival after acute myocardial infarction. *The New England Journal of Medicine* **319**, 1615-1622 (1993).
21. Lyden, P. D. *Thrombolytic Stroke Therapy, 2nd Edition* (Humana Press, New Jersey, 2004).
22. Skalak, R., Chen, P. H. & Chien, S. Effect of hematocrit and rouleaux on apparent viscosity in capillaries. *Biorheology* **9**, 67-83 (1972).

23. Goldman, D. & Popel, A. S. A computational study of the effect of capillary network anastomoses and tortuosity on oxygen transport. *Journal of Theoretical Biology* **206**, 181-194 (2000).
24. Schaffer, C. B. et al. Two-photon imaging of cortical surface microvessels reveals a robust redistribution in blood flow after vascular occlusion. *Public Library of Science, Biology* **4**, in press (2006).
25. Baron, J. C. Perfusion thresholds in human cerebral ischemia: Historical perspective and therapeutic implications. *Cerebrovascular Disease* **11**, 2-8 (2001).
26. Hossmann, K. A. Viability thresholds and the penumbra of focal ischemia. *Annals of Neurology* **36**, 557-565 (1994).
27. Zhao, W., Belayev, L. & Ginsberg, M. D. Transient middle cerebral artery occlusion by intraluminal suture II. Neurological deficits, and pixel-based correlation of histopathology with local blood flow and glucose utilization. *Journal of Cerebral Blood Flow and Metabolism* **17**, 1281-1290 (1997).
28. O'Brien, J. T. et al. Vascular cognitive impairment. *Lancet Neurology* **2**, 89-98 (2003).
29. Dobrogowska, D. H., Lossinsky, A. S., Tarnawski, M. & Vorbrodt, A. W. Increased blood-brain barrier permeability and endothelial abnormalities induced by vascular endothelial growth factor. *Journal of Neurocytology* **27**, 163-173 (1998).
30. Rosenberg, G. A., Mun-Bryce, S., Wesley, M. & Kornfeld, M. Collagenase-induced intracerebral hemorrhage in rats. *Stroke* **21**, 801-807 (1990).
31. Dijkhuizen, R. M., Asahi, M., Wu, O., Rosen, B. R. & Lo, E. H. Rapid breakdown of microvascular barriers and subsequent hemorrhagic transformation after delayed recombinant tissue plasminogen activator treatment in a rat embolic stroke model. *Stroke* **33**, 2100-2104 (2002).
32. Kaufman, H. H. et al. A rabbit model of intracerebral hematoma. *Acta Neuropathology (Berlin)* **65**, 318-321 (1985).
33. Fazekas, F. et al. Histopathologic analysis of foci of signal loss on gradient-echo T2*-weighted MR images in patients with spontaneous intracerebral hemorrhage: Evidence of microangiopathy-related microbleeds. *American Journal of Neuroradiology* **20**, 637-642 (1999).
34. Lyden, P. D., Jackson-Friedman, C., Shin, C. & Hassid, S. Synergistic combinatorial stroke therapy: A quantal bioassay of a GABA agonist and a glutamate antagonist. *Experimental Neurology* **163**, 477-489 (2000).
35. Zea Longa, E., Weinstein, P. R., Carlson, S. & Cummins, R. Reversible middle cerebral artery occlusion without craniectomy in rats. *Stroke* **20**, 84-91 (1989).
36. Wei, L., Rovainen, C. M. & Woolsey, T. A. Ministrokes in rat barrel cortex. *Stroke* **26**, 1459-1462 (1995).
37. Yao, H. et al. Photothrombotic middle cerebral artery occlusion and reperfusion laser system in spontaneously hypertensive rats. *Stroke* **34**, 2716-2721 (2003).
38. Nakase, H., Kakizaki, T., Miyamoto, K., Hiramatsu, K. & Sakaki, T. Use of local cerebral blood flow monitoring to predict brain damage after disturbance to the venous circulation: Cortical vein occlusion model by photochemical dye. *Neurosurgery* **37**, 280-285 (1995).
39. Takeo, S., Miyake, K., Minematsu, R., Tanonaka, K. & Konishi, M. In vitro effect of naftidrofuryl oxalate on cerebral mitochondria impaired by microsphere-induced embolism in rats. *Journal of Pharmacology and Experimental Therapeutics* **248**, 1207-1214 (1989).
40. Kudo, M., Aoyama, A., Ichimori, S. & Fukunaga, N. An animal model of cerebral infarction. Homologous blood clot emboli in rats. *Stroke* **13**, 505-508 (1982).
41. Futrell, N. et al. A new model of embolic stroke produced by photochemical injury to the carotid artery in the rat. *Annals of Neurology* **23**, 351-257 (1988).
42. Lo, E. H., Dalkara, T. & Moskowitz, M. A. Mechanisms, challenges and opportunities in stroke. *Nature Reviews of Neuroscience* **4**, 399-415 (2003).
43. Kleinfeld, D. & Delaney, K. R. Distributed representation of vibrissa movement in the upper layers of somatosensory cortex revealed with voltage sensitive dyes. *Journal of Comparative Neurology* **375**, 89-108 (1996).
44. Tsai, P. S. et al. in *In Vivo Optical Imaging of Brain Function* (ed. Frostig, R. D.) 113-171 (CRC Press, Boca Raton, 2002).
45. Tsai, P. S. et al. All-optical histology using ultrashort laser pulses. *Neuron* **39**, 27-41 (2003).
46. Backus, S. et al. High-efficiency, single-stage 7-kHz high-average-power ultrafast laser system. *Optics Letters* **26**, 465-467 (2001).

47. Zhang, R. L., Zhang, Z. G. & Chopp, M. Increased therapeutic efficacy with rt-PA and anti-CD18 antibody treatment of stroke in the rat. *Neurology* **15**, 273-279 (1999).
48. Korninger, C. & Collen, D. Studies on the specific fibrinolytic effect of human extrinsic (tissue-type) plasminogen activator in human blood and in various animal species in vitro. *Thrombosis and Haemostasis* **46**, 561-565 (1981).
49. Scremin, O. U. in *The Rat Nervous System* (ed. Paxinos, G.) (Academic Press, Inc., San Diego, 1995).

FIGURE LEGENDS

Figure 1. Experimental set-up. (a) Schematic of the two-photon laser scanning microscope modified for delivery of amplified ultrashort pulses for photodisruption. Low-energy, 100-fs, 80-MHz pulses for TPLSM were generated by a Titanium:Sapphire laser oscillator (Mira F-900; Coherent Inc.) that was pumped by a continuous wave (CW) laser (Verdi V-10 Nd:YVO_4 laser; Coherent Inc.). The imaging laser pulses were scanned in a raster pattern by galvanometric mirrors that are relay-imaged to the back aperture of the objective. The two-photon excited fluorescence is reflected by a dichroic mirror and relayed to a PMT. To produce laser pulses for photodisruption, we used a Pockels cell (QS-3 with NVP-525D driver and DD1 timing circuit; Quantum Technologies) to reroute 1 in 80,000 pulses from the oscillator pulse train to seed a multipass Titanium:Sapphire amplifier that is pumped by a Q-switched laser (Corona; Coherent). A half-wave plate ($\lambda/2$) rotates the polarization of the amplified pulses to lie perpendicular to that of the laser oscillator and thus allows both the photodisruption beam and the imaging beam to be routed to the microscope objective with a polarizing beamsplitter. **(b and c)** Maps of fluorescein-dextran labeled vasculature of rat parietal cortex. The inset in part **b** shows latex-filled surface arteries and arterioles in rat cortex (adapted from Scremin[49]) and the white rectangle indicates the approximate location of the craniotomy. The images in part **b** are a montage of maximal projections along the optical axis of near-surface vasculature; A↔P indicates the anterior-posterior axis and M↔L indicates the medial-lateral axis. A small region, indicated by the red box, was scanned at successive depths to form the maximal projection along A↔P, as indicated by the cartoon and shown in part **c**. The scale bar in part **b** is 500 μm, that in the insert is 5 mm, and that in part **c** is 100 μm. **(d)** Summary schematic of the three different vascular lesions that are produced by varying the energy and number of laser pulses. At high energies, photodisruption produces hemorrhages, in which the target vessel is ruptured, blood invades the brain tissue, and a mass of RBCs form a hemorrhagic core. At low energies, the target vessel remains intact, but transiently leaks blood plasma and RBCs forming an extravasation. Multiple pulses at low energy leads to thrombosis that can completely occlude the target vessel, forming an intravascular clot. The scale bar is 50 μm.

Figure 2. Hemorrhage via rupture of target vessel. (a) Maximal projections of TPLSM stacks in the vicinity of the target vessel before (left) and after (right) induction of a hemorrhage in a target vessel, 140 μm below cortical surface, by ultrashort laser pulses. After irradiation,

the target vessel is not observable. Fluorescently-labeled blood plasma invades the parenchymal tissue well beyond the extent of the dark spherical volume in the center. Cartoons on left indicate the directions and volumes of the maximal projections. **(b)** Temporal sequence of planar images during the formation of the hemorrhage shown in part **a**. The red pulse indicates irradiation with 8, 0.6-μJ, pulses delivered at 1 kHz. Time-zero is matched to that in part **c**. All images were spatially filtered to remove artifacts from pump laser light that leaked through the filters to the PMT, although amplified laser light leaked through and resulted in a series of bright dots in the panel at t = 1 s. The lines marked "r" and "h" indicate the measured radius of the extravasation of the fluorescein-dextran dye and the hemorrhage core, respectively. **(c)** Graphs of the distance from the center of the targetted vessel to the outer extents of both the core (green triangles) and the extravasated plasma (blue circles). The red pulse indicates the time of irradiation. **(d)** Volume of extravasated fluorescein versus target vessel diameter and the initial RBC speed. In both cases the regression coefficient is statistically insignificant. **(e to g)** Localization of a hemorrhage in a single coronal tissue section; the animal was sacrificed 40 minutes after the photodisruption of the blood vessel. Panel **e** shows the DAB-stained extravasated RBCs after immunolabeling the parenchyma with an antibody against MAP2. In part **f**, fluorescent imaging of fluorescein-dextran shows that extravasated blood plasma forms a halo that surrounds a central core of the hemorrhage. Part **g** is a high magnification view of the MAP2 labeled section within the box inset in parts **e** and **f**. Early pathology of somata are highlighted by the arrows while a normal neuronal soma is highlighted by lower asterisk; immunostaining preserved in a secondary apical dendritic structure is shown at upper asterisk.

Figure 3. Extravasation of blood constituents into the parenchymal tissue without obstruction of flow in target vessel. **(a)** Maximal projections of TPLSM stacks in the vicinity of the target vessel, located in the center of the field, before (left) and after (right) irradiation with high energy ultrashort laser pulses. The target vessel was 90 *μ*m below the cortical surface. Note that fluorescein-labeled blood plasma permeates a volume that surrounds the target vessel subsequent to irradiation. Cartoons on left indicate the directions and volumes of the maximal projections. **(b)** Temporal sequence of planar images through the center of the targeted vessel during the formation of the extravasation; the rectangle in part A (top left panel) shows the location of the field. Time-zero is matched to that in part **c**. Streaks visible in the vessel lumens were caused by RBC motion during the image acquisition and indicate blood flow. The line marked "r" indicates the measured radius of the extravasation of the fluorescein-

dextran dye. Images were spatially filtered to remove artifacts from Q-switched pump laser light leaking through the filters to the PMT. The red pulses denote epochs of irradiation with ~ 500, 0.3-μJ laser pulses delivered at 1-kHz. **(c)** Graphs of RBC speed (black triangles; left axis) and radius of extravasation (blue diamonds; right axis) during the irradiation of the target vessel. The red pulses indicate irradiation. The solid line indicates the average speed and the gray band marks the interval of ± 1 standard deviation. **(d)** Compilation of the volume of extravasation as a function of the vessel diameter, the initial RBC speed, and the depth of the targeted vessel. In all cases the regression coefficient is insignificant. **(e and f)** Photomicrographs of the site of extravasation in a single coronal section imaged with fluorescent illumination (part **e**) and bright field illumination (panel **f**); the animal was sacrificed 3 hours after the disruption. In part **e**, fluorescence of extravasated fluorescein-dextran fills a small area that lies deep to the pial surface. Part **f** illustrates focal accumulation of DAB stained RBCs as well as MAP2-immunostained neurons that are situated in close proximity to the clot.

Figure 4. Intravascular clot in intact target arteriole. (a) Maximal projections of TPLSM stacks in the vicinity of the target vessel before (left) and after (right) induction of an ischemic clot in the target vessel, 180 μm below the pial surface, by ultrashort laser pulses. The clot formation was accompanied by some extravasation. Cartoons on the left indicate the directions and volumes of the maximal projections. **(b)** Temporal sequence of planar images during the formation of the intravascular clot; the rectangle in the top left panel of part **a** shows the location of the field. The red pulses indicate irradiation with multiple trains of 0.03-μJ pulses delivered at 1 kHz. Time-zero is matched to that in part **c**. The panel at t = 60 s shows temporary cessation of RBC motion and swelling of the target vessel immediately after irradiation with 2 pulses. Flow resumed, as seen in the panel at t = 77 s. The vessel was then irradiated with 5 sets of 2 pulses, which lead to limited extravasation as seen in the panel at t = 230 s. Further irradiation with 5, 50-pulse trains caused further extravasation, as seen in the panel at t = 290 s. Final irradiation by 5, 10-pulse trains and 5, 100-pulse trains lead to clot formation and the stable cessation of RBC motion, as seen in the panel at t = 440 s. All images were spatially filtered to remove artifacts from pump laser light that leaked through the filters to the PMT. **(c)** Graph of RBC speed during the formation of a clot in the target vessel. Red pulses indicate irradiation with trains of laser pulses. **(d)** Histogram of the extravsation volumes, measured from the depth of the target vessel up to the surface and then doubled. **(e)** Compilation of the volume of extravasation measured as a function of the vessel diameter, the initial RBC speed, the depth of

the targeted vessel, and estimated laser pulse energy at the focus. The volume versus speed is fit with the function Volume/pl = 85 *exp*{speed/(5.2 mm/s)}, for which r = 0.5 with $p < 0.0001$.

Figure 5. Histological characterization of intravascular clots. (a to d) Localization of a clot in a single coronal tissue section; the animal was sacrificed 3 hours after the disruption. Parts **a** and **b** illustrate the aggregation of DAB stained RBCs in the vicinity of the targeted subsurface vessel in a section immunolabeled with an antibody against MAP2. The inset is a photomicrograph in the plane of the aggregate. In part **c**, fluorescent imaging of the same area in panel ii shows that the clot is also a site of extravasated fluorescein-dextran. Part **d** is a high magnification view just below the clot. Immunoreactivity shows minor, early pathology (arrows to angulated neurons) as well as predominantly normal somata (asterisks). **(e)** *In vivo* image, obtained with TPLSM of the clotted microvessel in a view tangential to the surface. The vessel is 250 μm deep to the pial surface. Subsequent immunolabeling of tissue from this animal, shown in parts **f** to **m**, involved pre-treatment with peroxide to eliminate staining of endogenous red blood cells. A dark reaction product is indicative of immunostained reaction product. The red ellipses in parts **f** to **m** delineate a common area in the vicinity of this clot. **(f to i)** Anti-fibrin immunostaining indicates localization of fibrin/fibrinogen clot markers (part **f**), which appears as a mixed diffuse zone from extravasated serum that surrounds a small dense region of intense staining. The latter region is shown at higher magnification in parts **h** and **i**. A mixed image of fluorescein-dextran vascular retention and the fibrin immunoreactivity (part **g**) indicates that the fibrin is confined to the immediate vicinity of the clot as marked by the territory of extravasated fluorescein. A high magnification image from the central zone of dense fibrin immunostaining (part **i**; focused below the surface of the tissue) show that dense labeling is associated with a vessel that is situated near the center of the fluorescein extravasation. **(j and k)** Immunolabeling of tissue with the reactive astrocyte marker vimentin did not appreciably increase the labeling of vessels just below the clot only. A mixed image of fluorescein-dextran retention and the vimentin immunoreactivity indicates that the damage is colocalized (part **k**). **(l and m)** The section, immunolabeled with an antibody against pimonidazole adducts (Hypoxyprobe™), shows that localization of adducts is weak and largely restricted to the vicinity of the clot. A mixed brightfield-fluorescent image shows that the fluroescein-dextran retained in the vessels and extravasated into the parenchyma overlaps the pimonidazole labeling (part **m**).

Figure 6. Changes in red blood cell velocity around subsurface intravascular clots. (a to c) Images of vasculature and schematic of blood flow around intravascular clots. Maximal projections of images before and after intravascular clot formation are shown in the 1st and 4th columns, respectively. The schematic indicates RBC velocity in vasculature before (2nd column) and after (3rd column) clot formation by ultrashort laser pulse irradiation. The location of the clot in a targeted vessel is marked by the red X. Negative numbers in red indicate vessels in which the flow direction reversed after clot formation. **(a)** Projections and schematic of flow, taken 90 to 200 μm below cortical surface, in the vicinity of a targeted arteriole. The asterisk indicates a downstream vessel whose flow was reversed by the clot but remains high. **(b)** Projections and schematic of flow in an arteriole that branches off of a diving arteriole, marked by black disc in the schematic, taken through cortex 300 to 400 μm below the pial. Note that the vessel farthest on the right is stalled before the clot, then flowing after the clot. Although this vessel is near the targeted vessel, it was not clotted by the laser irradiation of the neighboring vessel. The asterisk indicates a vessel whose flow was essentially unaffected by the clot. **(c)** Projections and schematic of flow, taken through the top 250 μm of cortex, in the vicinity of a targeted arteriole. The associated capillary network was fed by two surface arterioles that are indicated by the thick lines. **(d to g)** Compilation of RBC speeds in vessels connected with a clotted vessel before and after clot formation (132 vessels in 20 networks). The reported speed for each vessel was an average over 37 s. Different symbols indicate the measured vessel's connectivity relative to the clotted vessel (part **d**). Standard error of the mean of the measurements are approximately the size of a symbol in the graph. The diagonal lines indicate equal post-clot and baseline magnitudes. The insert for D1 and D2 branches shows a larger dynamic range.

Figure 7. Changes in RBC velocity around an intravascular clot with hemodilution. The velocities of RBCs were measured before and after clot formation and after hemodilultion by intravenous saline. **(a)** Red blood cell velocities at baseline, after occlusion, and after hemodilution in an example network. Red X marks the occluded vessel, and vessels in which blood flow reversed direction after occlusion are indicated in red. **(b)** Compilation of RBC speeds in classes of vessels (part **d**) that lie downstream from an occluded vessel prior to clot formation (baseline), after photo-induced occlusion (clot) and after hemodilution (dilution). Negative velocities indicate that the flow reversed in direction relative to baseline. **(c)** Compilation of RBC speeds in control vessels with similar size and speed as non-control

vessels but which were fed by a different diving arteriole. These vessels were 300 μm to 1 mm away from the target vessel. **(d)** Bar graph showing the differences in RBC velocity, v_{clot} - $v_{baseline}$ (dark bars) and $v_{dilution}$ - v_{clot} (white bars), together with one SEM error bars.

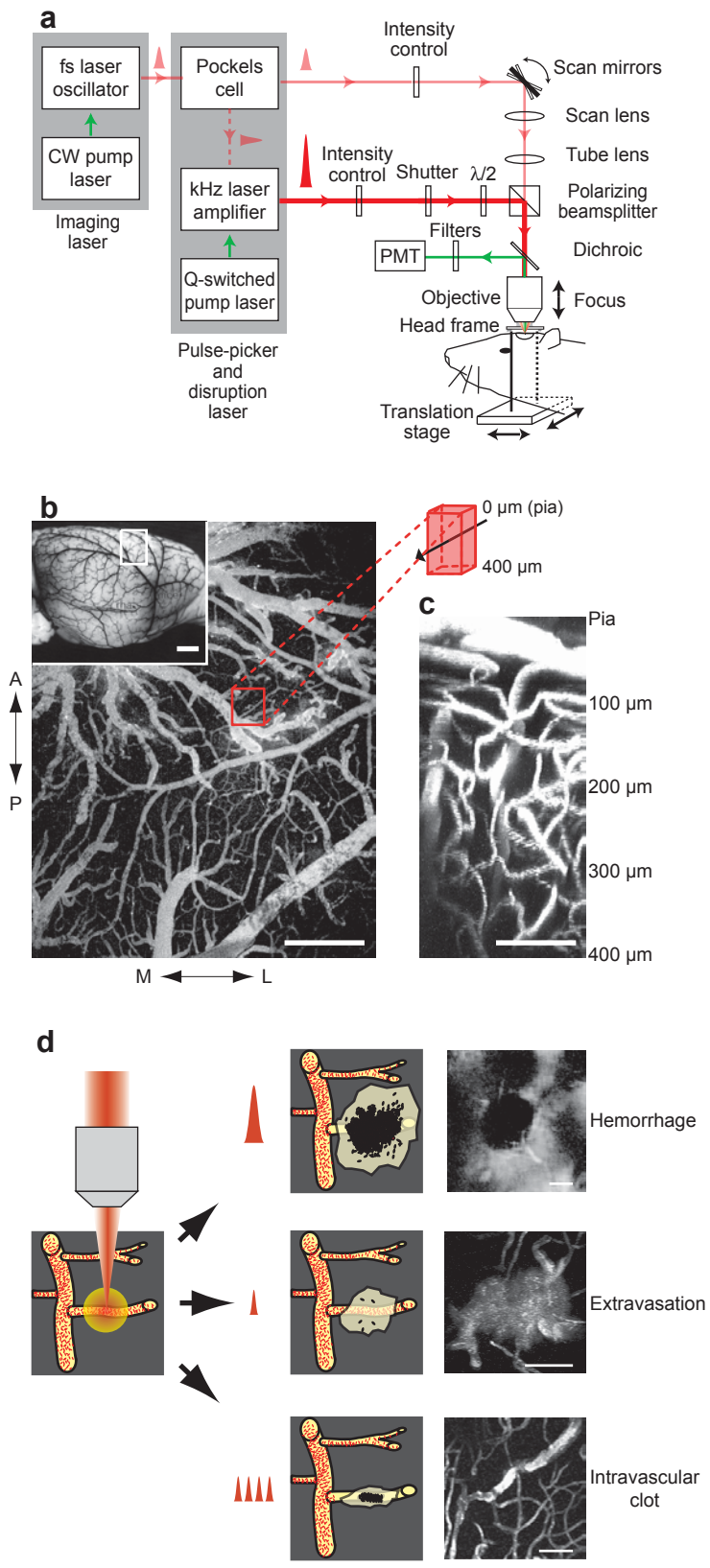

Figure 1 - Nishimura, Schaffer, Friedman, Tsai, Lyden and Kleinfeld

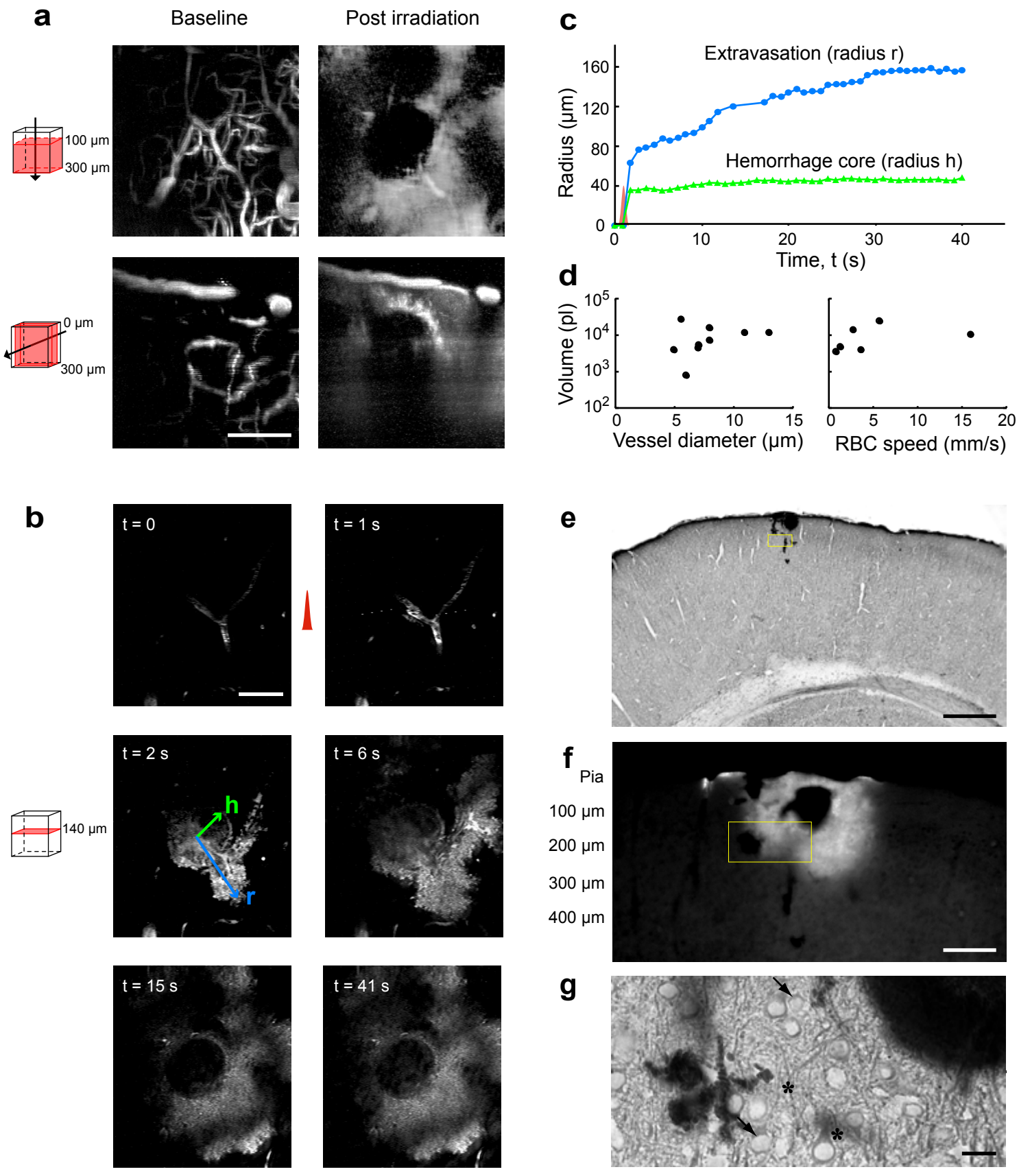

Figure 2 - Nishimura, Schaffer, Friedman, Tsai, Lyden and Kleinfeld

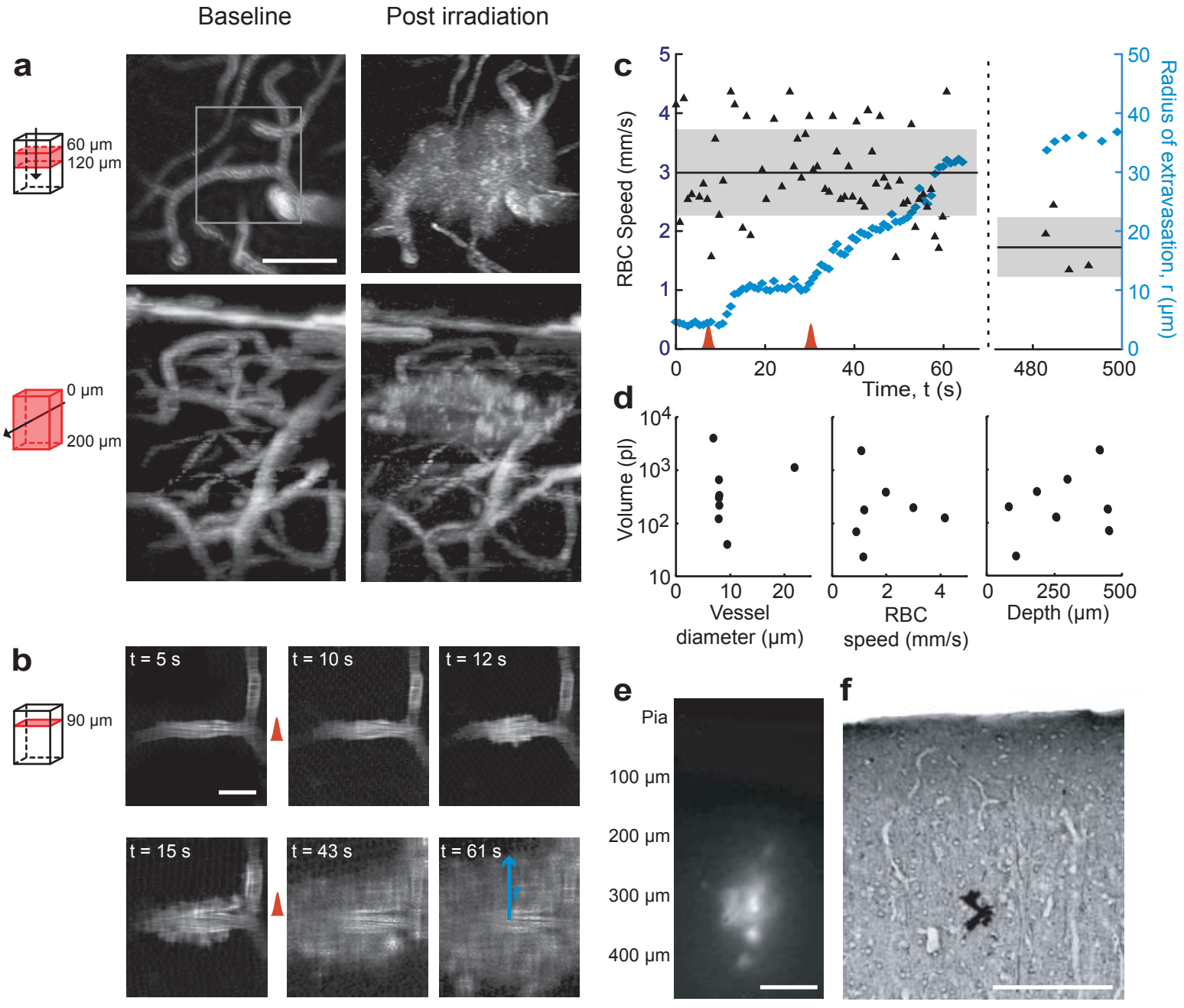

Figure 3 - Nishimura, Schaffer, Friedman, Tsai, Lyden and Kleinfeld

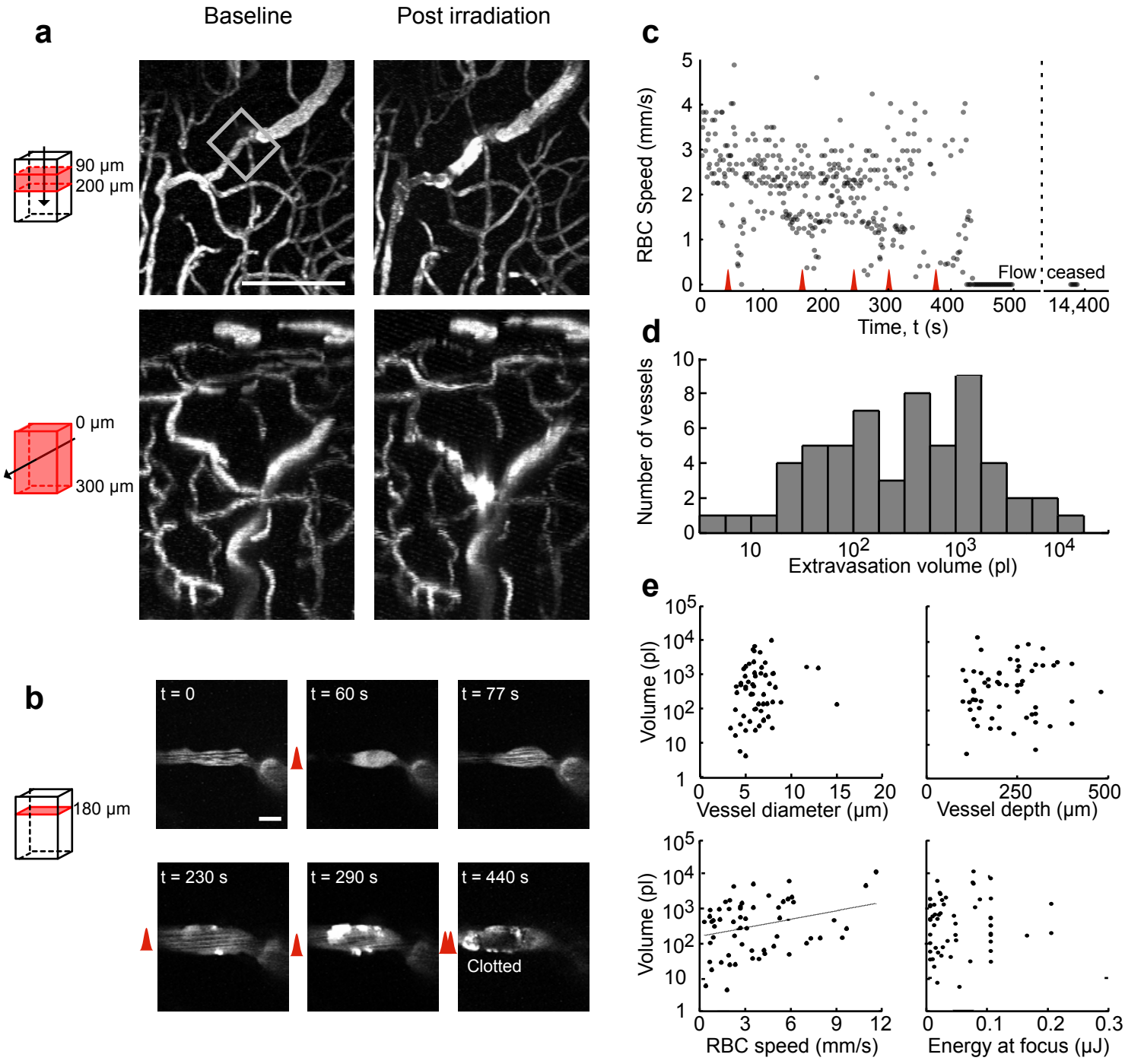

Figure 4 - Nishimura, Schaffer, Friedman, Tsai, Lyden and Kleinfeld

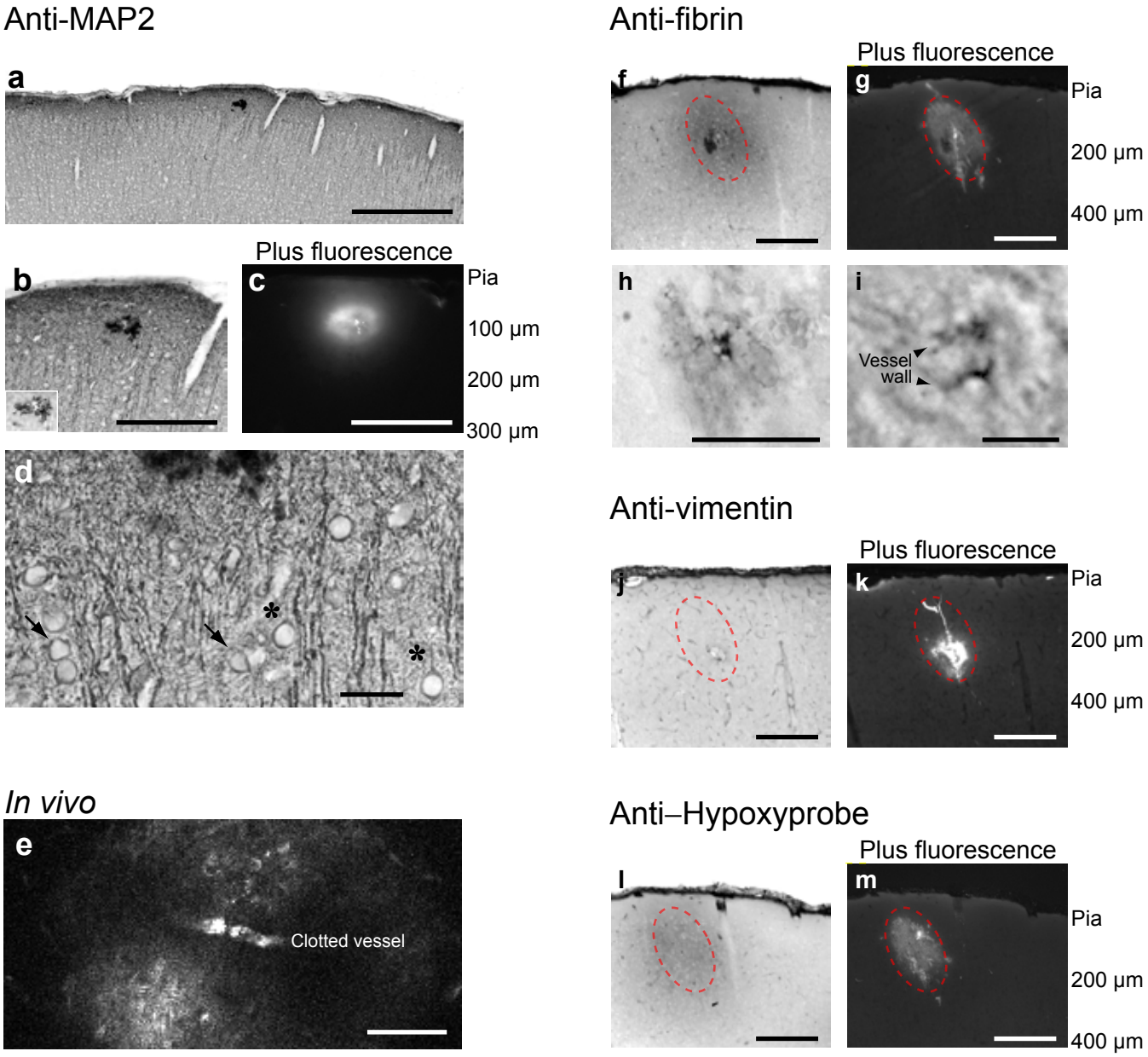

Figure 5 - Nishimura, Schaffer, Friedman, Tsai, Lyden and Kleinfeld

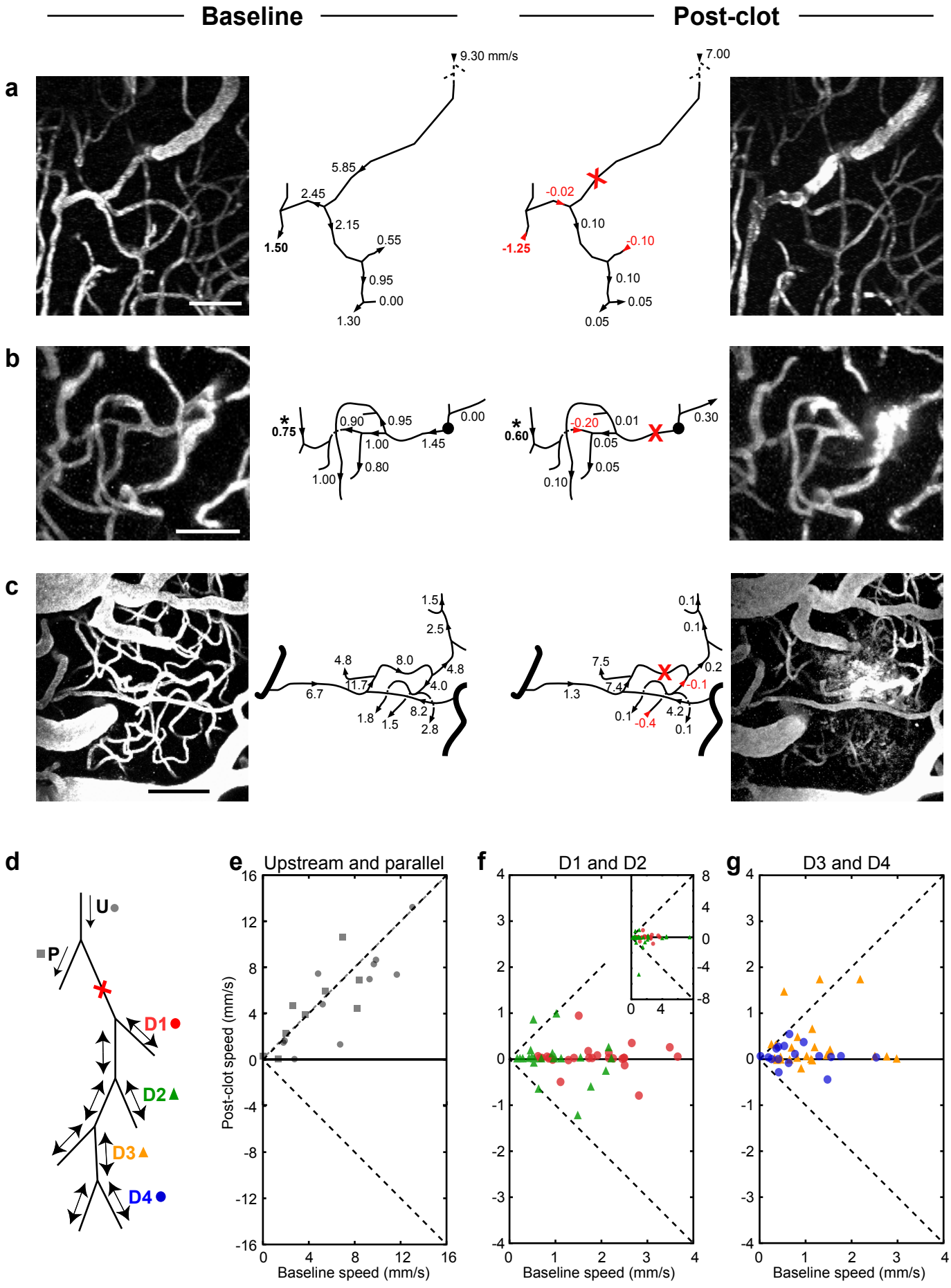

Figure 6 - Nishimura, Schaffer, Friedman, Tsai, Lyden and Kleinfeld

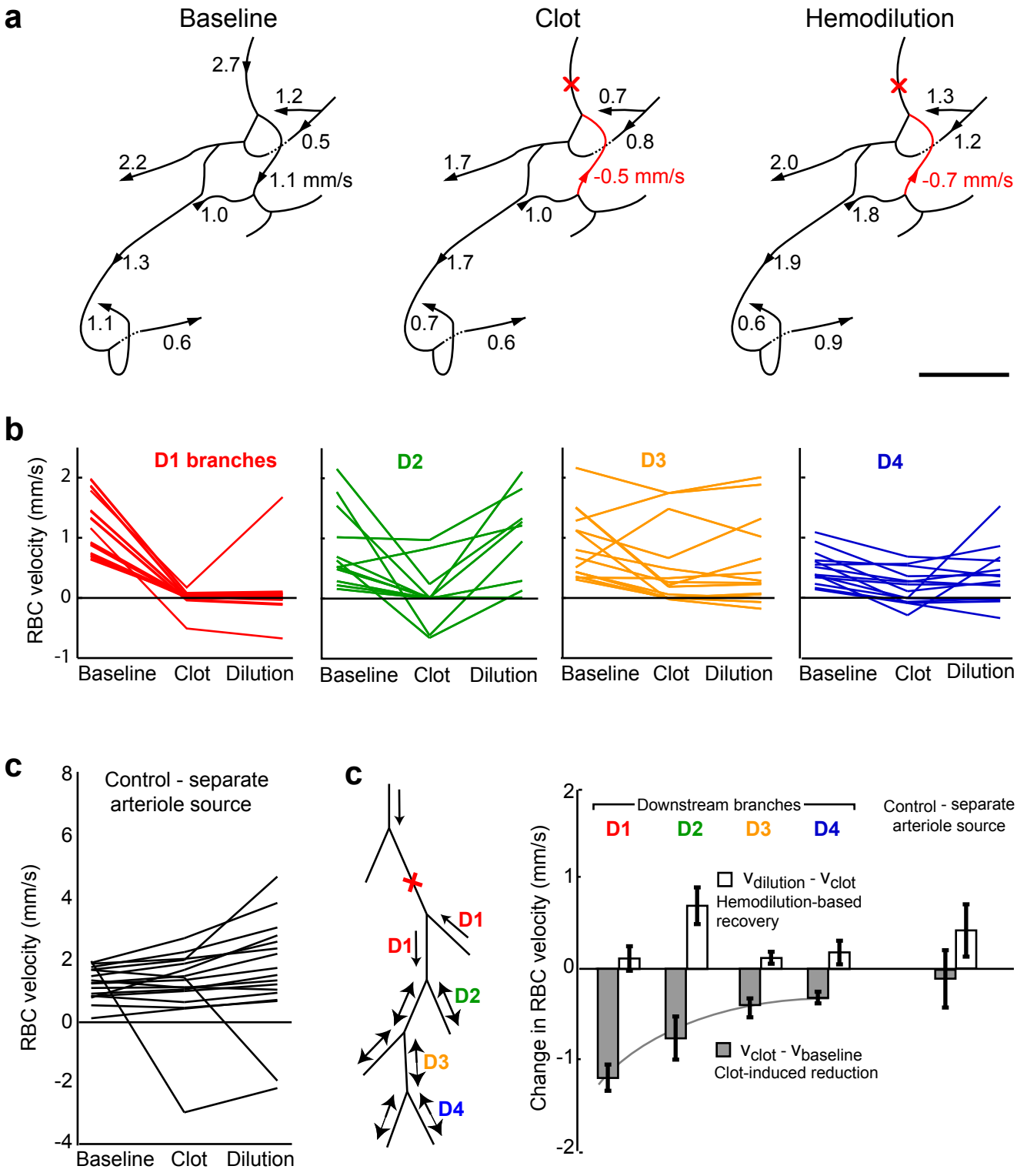

Figure 7 - Nishimura, Schaffer, Friedman, Tsai, Lyden and Kleinfeld

SUPPLEMENTAL MATERIAL

"Targeted insult to individual subsurface cortical blood vessels using ultrashort laser pulses: Three models of stroke" by N. Nishimura, C. B. Schaffer, B. Friedman, P. S. Tsai, P. D. Lyden and D. Kleinfeld

SUPPLEMENTAL METHODS

Estimation of extravasation volume

Volumes were determined from stacks of *in vivo* TPLSM images. Planes that spanned 5 μm were averaged. The extravasation volume was estimated by counting pixels with intensities greater than 10% of the range of intensities in the spatially averaged image. To ensure similar intensity distributions across image stacks, only image stacks in which vessels outside the extravasation volume equaled the maximum intensity values were used. We only measured the volume of the top half of the extravasation, since many target vessels were near the maximum imaging depth, and doubled this value.

Post mortem analysis

At the end of each experiment, animals were deeply anesthetized and perfused with 100 ml of phosphate buffered saline (PBS), followed by 150 ml of 4 % (w/v) paraformaldehyde in PBS. The glass coverslip and agarose covering the cranial window were removed and electrolytic fiducial marks were made in the corners of the craniotomy by driving a single tungsten electrode into the brain (no. WE3003(2-5)A10; MicroProbe) at a speed of ~ 0.2 mm/s while passing a current of ~ -20 μA. The brains were then removed from the skull, post-fixed in 4 % (w/v) paraformaldehyde in PBS, cryoprotected by equilibration in 30 % (w/v) sucrose in PBS, and cut on a freezing-sliding microtome into 50-μm coronal sections. The sections were incubated with diaminobenzadine (DAB) to stain endogenous peroxidase in RBCs. The sections were wet-mounted on glass slides and photographed with brightfield and epifluorescence microscopy. Vascular disruptions could be identified on the basis of both fluorescein-dextran extravasation[1,2] and DAB stained RBCs and were mapped relative to the location of the electrolytic fiducials.

Hypoxyprobe. Six of the animals received injections of pimonidazole hydrochloride (Hypoxyprobe-1™) (90201; Chemicon) 1 hour before sacrifice. These animals were sacrificed and perfused as above and histological sections were prepared.

Immunohistochemistry. Sections with documented vascular disruption were dried onto glass slides (Superfrost Plus; Fisher) and underwent antigen retrieval in 10 mM citrate buffer, pH 6.0, heated to boiling in a microwave oven (300 s at full power). The slides were incubated overnight in one of four monoclonal antibodies in diluent with PBS and 0.2 % (v/v) Triton X–100 followed by incubation with a biotinylated anti-mouse secondary antibody: (*i*) Hypoxyprobe™ antibody (90204; Chemicon); (*ii*) MAP2 antibody (M1406; Sigma); (*iii*) fibrin antibody (MAB1901; Chemicon); and (*iv*) vimentin antibody (MAB3400; Chemicon). In all cases bound antibody was visualized with the Vector ABC Kit (no. PK6100) using DAB (no. DAB; Vector) as the chromagen. The sections were cover-slipped with Prolong mountant (no. 36930; Molecular Probes).

We checked for nonspecific antibody staining. A photomicrograph, obtained at low magnification, illustrates that the staining with anti-fibrin and visualization with DAB leads to a locally defined dark product and the remainder of the section essentially negative (Fig. S1).

MECHANISM FOR VASCULAR INSULT WITH ULTRASHORT LASER PULSES

At energies above the threshold for optical breakdown, past studies show that the absorption of ultrashort laser pulses leads to the formation of a cavitation bubble and a shock wave[3-8]. At energies well above the threshold for breakdown, the size of cavitation bubbles can approach the size of the core of a hemorrhage (Fig. 2). The hemorrhage core could be formed by RBCs and blood plasma from the ruptured vessel that fill in a volume disrupted by the rapid expansion of the cavitation bubble. Thus, in vessel rupture, the spherical feature that is observed by TPLSM immediately after photodisruption may be representative of the maximum radius of a cavitation bubble

(Fig. 2B, panel ii). We found that the volume of the hemorrhage core, denoted v, scales with the estimated laser pulse energy at the focus in the *in vivo* brain, according to the phenomenological relation (Fig. S2):

$$v \simeq \left(280\ \text{pL}\right)\ e^{\frac{E_{focus}}{0.15\ \mu J}}$$

where E_{focus} is the energy at the focus and the fit is valid ($p < 0.01$) for $0.05\ \mu J < E_{focus} < 0.3\ \mu J$. The energy at the focus is decreased by absorption and scattering in comparison with the incident energy, denoted $E_{incident}$, and can be approximated by an exponential dependence on depth, z, with an attenuation length, Λ, *i.e.*,

$$E_{focus} \simeq e^{-z/\Lambda}\ E_{incident}\ .$$

We take an attenuation length of $\Lambda \approx 200$ μm as representative of values found in the literature[9-11] and neglect optical aberrations. In contrast, the volume of fluorescently-labeled plasma extravasation does not correlate with laser energy suggesting that the plasma extravasation may be dependant on local tissue properties rather than laser parameters.

The energies used to yield the extravasations (Fig. 3) and the intravascular clots (Fig. 4) are nearer the threshold for photodisruption and lower than those that yield vessel ruptures (Fig. 2). At low energies, several effects act to limit tissue damage so that the mechanical events that follow irradiation may only partially disrupt vessels and thus minimally affect the surrounding tissue. First, a smaller fraction of the laser pulse is absorbed at laser pulse energies near threshold than at energies substantially above threshold[12]. Thus the fraction of energy available for cavitation bubble formation and damage by shock waves is likely to be less in the cases of extravasations and clots, which occur near threshold, compared to that for vessel ruptures. Second, the velocity and pressure of the shock wave decreases rapidly with radius from the center of the photodisruption[4,13,14]. Thirdly, the cavitation bubble and shock wave are likely to induce circumferential strain in the vessel wall. Thus, vascular cells that wrap around the target vessel, *e.g.,* endothelial cells, are likely preferentially damaged by photodisruption when compared to cells that abut the vessel.

References

1. Zhang, Z., Davies, K., Prostak, J., Fenstermacher, J. & Chopp, M. Quantitation of microvascular plasma perfusion and neuronal microtubule-associated protein in ischemic mouse brain by laser-scanning confocal microscopy. *Journal of Cerebral Blood Flow and Metabolism* **19**, 68-78 (1999).
2. Lindsberg, P. J., Siren, A. L. & Hallenbeck, J. M. Microvascular perfusion during focal vasogenic brain edema: A scanning laser fluorescence microscopy study. *Microvascular Research* **53**, 92-103 (1997).
3. Schaffer, C. B., Nishimura, N., Glezer, E. N., Kim, A. M. T. & Mazur, E. Dynamics of femtosecond laser-induced breakdown in water from femtoseconds to microseconds. *Optics Express* **10**, 196-203 (2002).
4. Juhasz, T., Kastis, G. A., Suarez, C., Bor, Z. & Bron, W. E. Time-resolved observations of shock waves and cavitation bubbles generated by femtosecond laser pulses in corneal tissue and water. *Lasers in Surgery and Medicine* **19**, 23-31 (1996).
5. Vogel, A. & Venugopalan, V. Mechanisms of pulsed laser ablation of biological tissues. *Chemical Reviews* **103**, 577-644 (2003).
6. Joglekar, A. P., Liu, H. H., Meyhofer, E., Mourou, G. & Hunt, A. J. Optics at critical intensity: Applications to nanomorphing. *Proceedings of the National Academy of Sciences USA* **101**, 5856-5861 (2004).
7. Stuart, B. C., Feit, M. D., Herman, S., Rubenchik, A. M., Shore, B. W. & Perry, M. D. Nanosecond-to-femtosecond laser-induced breakdown in dielectrics. *Physical Review B* **53**, 1749-1761 (1996).
8. Loesel, F. H., Fischer, J. P., Gotz, M. H., Horvath, C., Juhasz, T., Noack, F., Suhm, N. & Bille, J. F. Non-thermal ablation of neural tissue with femtosecond laser pulses. *Applied Physics B* **66**, 121-128 (1998).
9. Yaroslavsky, A. N., Schulze, P. C., Yaroslavsky, I. V., Schober, R., Ulrich, F. & Schwarzmaier, H. J. Optical properties of selected native and coagulated human brain tissues in vitro in the visible and near infrared spectral range. *Physics in Medicine and Biology* **47**, 2059-2073 (2002).
10. Kleinfeld, D., Mitra, P. P., Helmchen, F. & Denk, W. Fluctuations and stimulus-induced changes in blood flow observed in individual capillaries in layers 2 through 4 of rat neocortex. *Proceedings of the National Academy of Sciences USA* **95**, 15741-15746 (1998).
11. Oheim, M., Beaurepaire, E., Chaigneau, E., Mertz, J. & Charpak, S. Two-photon microscopy in brain tissue: Parameters influencing the imaging depth. *Journal of Neuroscience Methods* **111**, 29-37 (2001).
12. Schaffer, C. B., Nishimura, N. & Mazur, E. in *International Society for Optical Engineering (SPIE)* 2-8 (Proceedings of International Society for Optical Engineering, 1998).
13. Noack, J. & Vogel, A. Single-shot spatially resolved characterization of laser-induced shock waves in water. *Applied Optics* **37**, 4092-4099 (1998).
14. Maatz, G., Heisterkamp, A., Lubatschowski, H., Barcikowski, S., Fallnich, C., Welling, H. & Ertmer, W. Chemical and physical side effects at application of ultrashort laser pulses for intrastromal refractive surgery. *Journal of Optics A* **2**, 59-64 (2000).

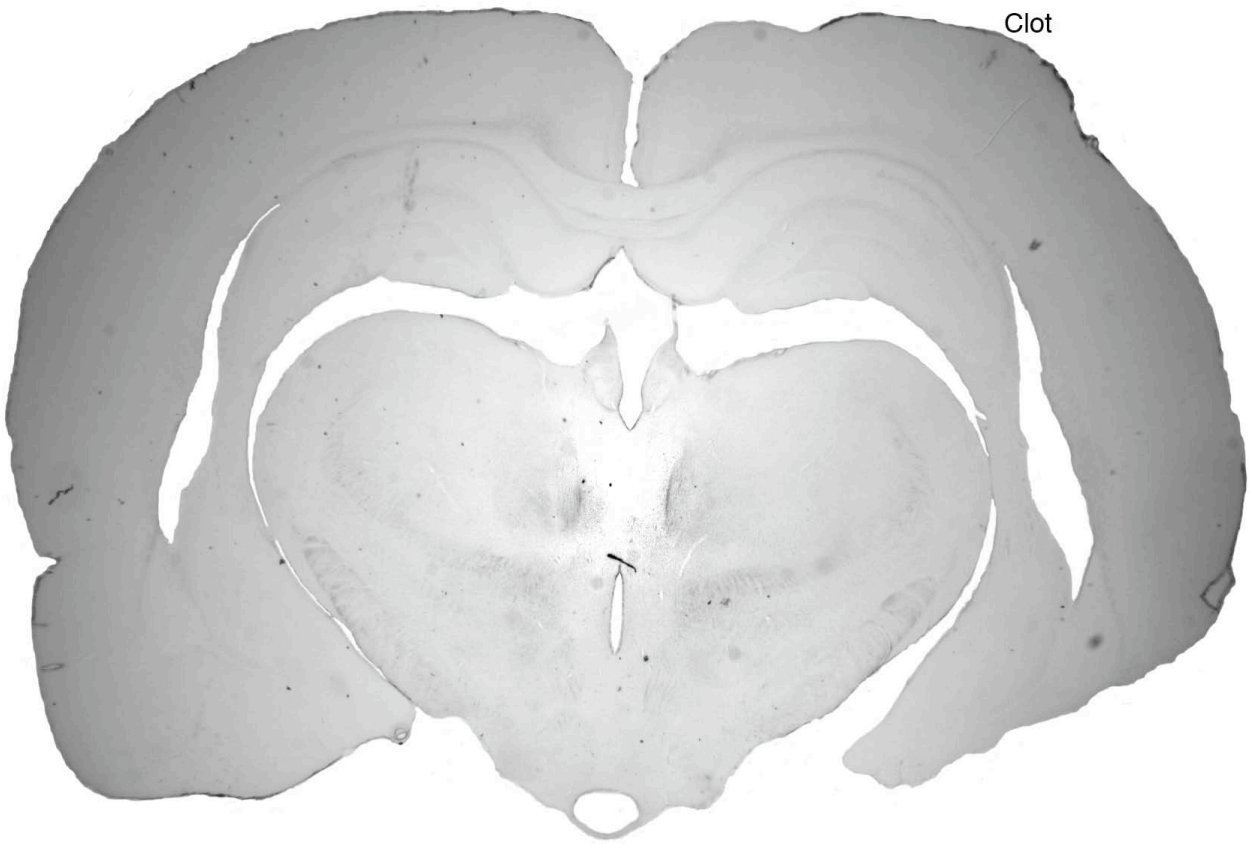

Figure Supplement 1. Anti-fibrin immunostaining indicates localization of fibrin/fibrinogen clot marker (Clot). This is the full section used for figure 5B2. Note that some dirk marks are present in the section.

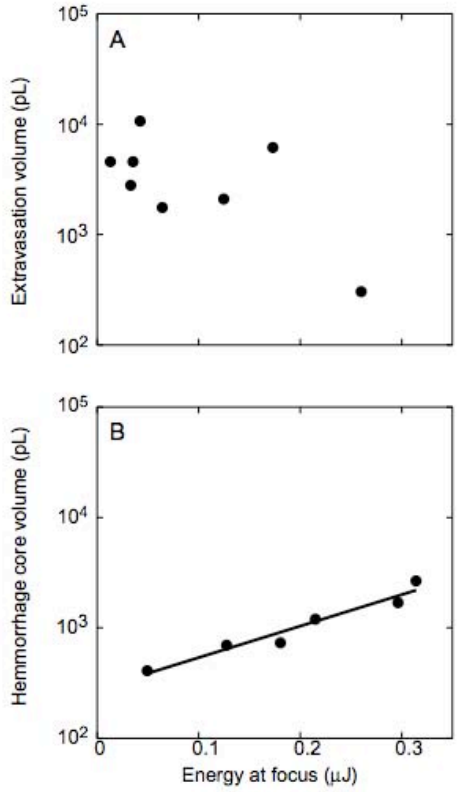

Figure Supplement 2. Hemorrhage size versus laser pulse energy at focus. (A) Extravasation volume as measured in *in vivo* TPLSM image stacks. **(B)** Hemorrhage core radii were measured in TPLSM images of vessel rupture formation within 1 s after photodisruption.